University of Birmingham

Compact Monolithic 3D-Printed Wideband Filters Using Pole-Generating Resonant Irises

Qian, Lu; Martinez, Rafael; Salek, Milan; Skaik, Talal; Attallah, Moataz; Wang, Yi

[Link to publication on Research at Birmingham portal](#)

IEEE Journal of
Microwaves

Compact Monolithic 3D-Printed Wideband Filters Using Pole-Generating Resonant Irises

LU QIAN [1] (Graduate Student Member, IEEE), RAFAEL MARTINEZ[2], MILAN SALEK [1], TALAL SKAIK [1], MOATAZ ATTALLAH [2], AND YI WANG [1] (Senior Member, IEEE)

[1]EDT Laboratory, School of Engineering, University of Birmingham, B15 2TT Birmingham, U.K.
[2]School of Metallurgy and Materials, University of Birmingham, B15 2TT Birmingham, U.K.

CORRESPONDING AUTHOR: Yi Wang (e-mail: Y.Wang.1@bham.ac.uk).

ABSTRACT The design concept of a pole-generating resonant iris is demonstrated in rectangular waveguide filters in this paper. Different from conventional reactive iris, the resonant iris can generate an extra transmission pole without increasing the number of resonant cavities. As a result, several design advantages can be gained: (i) a more compact filter structure; (ii) an ability to realize strong coupling and therefore wide bandwidth; and (iii) a new polarization rotation capability. Two third-order Chebyshev filters are designed and implemented, demonstrating the miniaturization and polarization rotation feature. A fifth-order Chebyshev filter with 20% fractional bandwidth is presented to show the capability of realizing wideband. This also demonstrates the realization of asymmetric coupling between the resonant iris and the cavity resonator on either side. An approach to control and extract the coupling between the iris and the cavity resonator has also been presented. To manufacture the intricate asymmetric iris structure, all the presented filters are printed monolithically using selective laser melting technique. Excellent agreement between the measurements and simulations has been achieved, verifying the design concept as well as the additive manufacturing capability in microwave waveguide devices.

INDEX TERMS Additive manufacturing (AM), evanescent mode, J-inverter, K-inverter, resonant iris, selective laser melting (SLM), waveguide filters, waveguide twists, wideband filter.

I. INTRODUCTION

Waveguide cavity filters have been widely used in satellite and base station applications because of their excellent performance in terms of low loss and high-power handling capacity. The rapid development of wideband communication and carrier aggregation has spurred the growing research activity in wideband waveguide filters [1], [2]. Typical filter requirements for 5G sub-6 GHz system are wideband (around 10%), compact in size, and low profile. In satellite communication transponders, wideband filters are often an indispensable part of the transmit–receive diplexers.

For waveguide filters, there are two typical approaches to realize wideband filtering performance. The first one requires cascading several coupled single-mode resonators [3], [4], [5], [6]. However, the increasing size and mass is a well-known concern as the order of waveguide filter rises. Wider

bandwidth usually needs stronger coupling. The irises that enable strong coupling strength are often associated with the degradation of out-of-band performance due to the higher-order modes and iris resonances. To address this drawback, one method is to push the iris resonance to higher frequency by dividing the single iris to multiple smaller apertures [7], but the coupling strength will decrease. Another approach to realizing wideband filter is to use multi-mode resonators [1], [8], [9], where multiple resonance modes were excited in a single resonator. The overall filter size can hence be reduced while the filter bandwidth can be increased. However, it is often difficult to implement the high-order filters because of the complicated coupling scheme. Filters with multi-mode resonators are also more sensitive to manufacturing tolerances and often suffer from poor temperature stability [10]. In practical filter applications, waveguide filters with explicit

coupling schemes and in-line configurations are still highly desirable.

Waveguide cavity filters usually use coupling irises (thin metallic diaphragms containing a concentric opening) to realize the coupling between cavities. From the circuit point of view, the irises can be normally represented as coupling capacitor or inductor. In the past decades, researchers have modified the coupling irises for new or enhanced functionalities in filters. In [11], [12], [13], capacitive and inductive irises were combined to implement a resonator to replace the waveguide cavity resonators, but the coupling between resonators relies on additional quarter wavelength waveguide inverters, which increases the size of the filter. In [14], [15], [16], [17], the frequency-dependent coupling irises were used to generate transmission zeros (TZs). More recently, iris structures have been used to realize multiple passbands or enhance the bandwidth of waveguide filters [18], [19]. However, it should be noted that all above function-enhancing irises rely on complex iris structures. Therefore, a capable and reliable fabrication solution will be the critical enabler to exploit the potential of the resonant iris and new iris structures.

These novel irises structures are traditionally manufactured in separate piece-parts by computer numerical control (CNC) machine and then bolted together [11], [12], [13], [17]. They could also be integrated into the filter, and the entire filter is machined out of multiple parts [15], [16], [19]. However, assembly error is an important source of performance degradation. The passive intermodulation (PIM) product generated at mechanical interconnections could reduce the power handling capacity. Moreover, the low manufacture freedom of conventional subtractive process severely limits the design flexibility of iris structures. Most previous work only look at rectangular resonant irises or non-centered resonant apertures.

In recent years, additive manufacture (AM) technology (known also as 3-D printing) becomes an increasingly popular method to construct microwave devices, because of its high freedom of rapid prototyping and the unique capability of forming complex geometric structures [20], [21], [22], [23], [24]. For instance, microwave filters based on non-conventional geometries have been designed and manufactured [25], [26], [27]. Monolithic waveguide subsystems that integrate several RF functionalities were reported [28], [29], [30]. Work to explore the printing of novel materials such as Invar can also been found in [31], [32].

We have recently proposed a 3-D printed waveguide filter using pole-generating resonant iris structure in [33]. By replacing the conventional reactive irises with resonant irises, an extra transmission pole (TP) can be implemented within the space previously occupied by the coupling iris. This allows a higher-order filter without excessive size increase. Selective laser melting (SLM) technique was employed to manufacture the unconventional resonant iris structures. Here we have extended the work in [33] in several areas: (1) Asymmetric coupling resonant iris was implemented, only enabled by the manufacturing capability of 3D printing. A new geometrical freedom was introduced to realize the asymmetric coupling on either side of the resonant iris, which is often impractical for
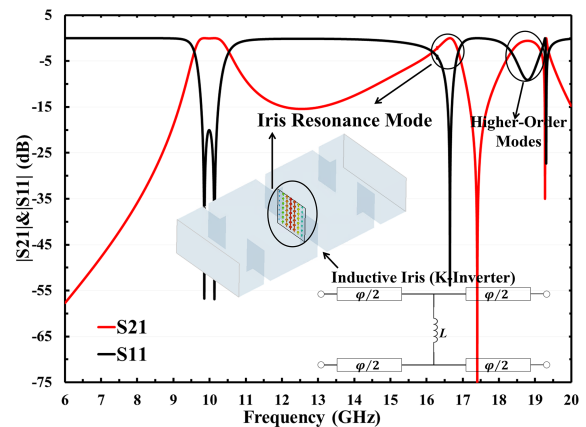

FIGURE 1. Frequency response of a two-pole coupled cavity filter using inductive irises, with inset showing the E-field pattern at the Iris projected on the middle cross-section.

traditional machining methods due to the limited lateral space within the iris. (2) Circuit analysis of the pole-generating resonant iris structure was presented. The frequency dependance of the iris coupling and the iris resonance feature were discussed. An intuitive design procedure was introduced. (3) The wideband capability was explored. A filter with 20% fractional bandwidth is demonstrated. (4) The polarization rotation capability, enabled by the symmetry in the resonant iris structure, was demonstrated. This allows a 90° twist to be easily embedded into the filter. Compared with traditional waveguide twists [34], [35], [36], this design feature eases the fabrication and provides a compact configuration. (5) The reproducibility of the SLM manufacture solution was investigated. Several designed filters were reproduced and measured. Measurement results show a good correlation with the tolerance analysis. This work also gives an assessment to the surface finish, by providing surface roughness measurements and showing the impact on insertion losses.

II. POLE-GENERATING RESONATING IRIS
A. CONCEPT OF POLE-GENERATING RESONANT IRIS
The initial idea of this design concept comes from a common phenomenon. The inductive coupling irises often accompany by a spurious resonance above the passband, deteriorating the out-of-band rejection, especially for wideband filters. Fig. 1 shows the frequency response of a waveguide filter with inductive irises and the TE_{101}-like electric field pattern of the iris when it resonates. In this work, we try to leverage the iris resonance and propose the pole-generating resonant iris structure. Fig. 2(a) shows the initial L-shaped resonant iris proposed in [33]. To form the resonant iris, an extra metallic diaphragm was added next to the symmetric inductive iris. Since the diaphragm introduces discontinuity into both the H-plane and E-plane, an L-shaped resonant aperture is realized. For comparison, the classic rectangular resonant iris is also presented in Fig. 2(b). From the simulated electric field (E-field) distributions, it is clear that both field patterns are like the TE_{101} mode, but the pattern of the L-shaped aperture is folded. Hence, the L-shaped resonant iris has a longer
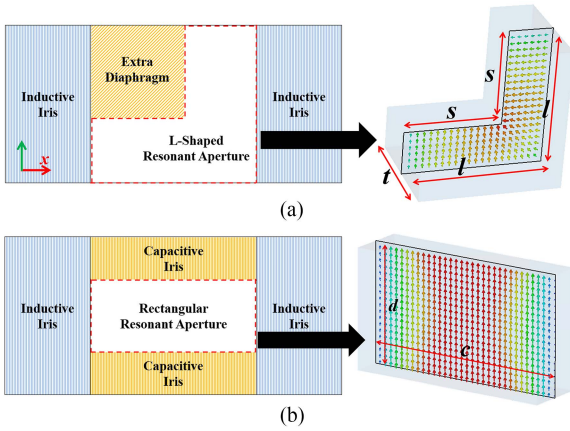
FIGURE 2. (a) L-shaped resonant Iris. (b) Rectangular resonant Iris. Front view of the structure (the left). E-field pattern of its resonance mode projected on the E-plane (the right).
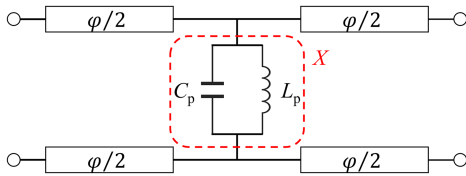

FIGURE 3. Equivalent circuit for the resonant Iris.

electrical length than the classic rectangular resonant iris. The iris resonance mode can be readily lowered into the passband, while the condensed E-field also enables the stronger coupling. Nevertheless, the above L-shaped iris can only realize basic pole-generating feature. To implement higher-order filters, a design methodology is needed. Therefore, the circuit analysis and electromagnetic optimization will be discussed next.

B. CIRCUIT MODEL AND ANALYSIS

The circuit model will be first illustrated to help understand the operation mechanism of the resonant iris. This circuit analysis will focus on the pole-generating feature. The inductive iris in Fig. 1 works as an impedance inverter (K-inverter) between two resonators and usually is represented as a shunt inductor as shown in the inset. However, the iris is a distributed physical structure. Its intrinsic frequency dependence will lead to unintended transmission feature. Herein, its embodiment is the extra transmission pole (TP) generated by the iris resonance mode on the upper stopband. To investigate the pole-generating feature, a resonant equivalent circuit was used, as presented in Fig. 3. The shunt inductor in the classical K-inverter is replaced by a parallel LC circuit, and its resonance frequency is determined by

$$\omega_P = 1/\sqrt{L_P C_P} \tag{1}$$

We will consider the following two cases:

1) CASE I: ($\omega_P \neq \omega_0$ WHERE ω_0 IS THE CENTER FREQUENCY OF THE FILTER)

In this case, the resonant iris amounts to a frequency-variant coupling element, which can offer the required coupling at the centre frequency while generate an extra transmission pole on the upper stopband. Considering the circuit in Fig. 3, the parallel LC can be regarded as a shunt reactance, X at ω_0, and the two-port network acts as a K-inverter. Two conditions can be imposed: 1) The parallel LC circuit resonates at ω_p ($\omega_p > \omega_0$); 2) At ω_0, the transmission matrix of the iris must be the same as that of the K-inverter. i.e.,

$$\begin{bmatrix} A & B \\ C & D \end{bmatrix} = \begin{bmatrix} 0 & -jK \\ 1/jK & 0 \end{bmatrix} \tag{2}$$

The elements of this matrix can be respectively calculated [37]:

$$A = D = \cos\varphi + \frac{Z_0}{2X}\sin\varphi$$

$$B = jZ_0\sin\varphi + j\frac{Z_0^2}{X}\sin^2\left(\frac{\varphi}{2}\right)$$

$$C = \frac{j}{Z_0}\sin\varphi + \frac{\cos^2\left(\frac{\varphi}{2}\right)}{jX} \tag{3}$$

where Z_0 is the characteristic impedance and X is the equivalent reactance of the parallel LC circuit at ω_0.

$$X = \frac{\omega_0 L_P}{1 - \omega_0^2 L_P C_P} \tag{4}$$

Combining (1)–(4), we can find

$$K = Z_0\tan\left|\frac{\varphi}{2}\right|, \varphi = -\arctan\frac{2X}{Z_0}$$

$$|X| = \frac{K}{1 - \left(\frac{K}{Z_0}\right)^2}, X = \frac{\omega_p^2\omega_0 L_P}{\omega_p^2 - \omega_0^2} \tag{5}$$

Therefore, for waveguide iris filters, once the passband specification is specified, we can predict the position of the transmission pole from the iris resonance, which can also provide insight for the achievable bandwidth of the designed waveguide filter. The corresponding shunt capacitor and inductor values can be further calculated using the following equation.

$$C_P = \frac{\omega_0\left(1 - (K/Z_0)^2\right)}{K\left(\omega_P^2 - \omega_0^2\right)}, X = \frac{\omega_p^2\omega_0 L_P}{\omega_p^2 - \omega_0^2} \tag{6}$$

To verify the circuit model, we consider the two-pole Chebyshev waveguide iris filter in Fig. 1. Its centre frequency and bandwidth with 20 dB return loss is 10 GHz and 400 MHz, respectively. Fig. 4 presents two schematic circuits for this filter, respectively based on the ideal K-inverter and the resonant inverter model, where $\omega_0 = 1/\sqrt{L_0 C_0}$. The circuit elements can be calculated to be: $C_0 = 0.151$ pF, $L_0 = 1.671$ nH, $K_{01} = K_{23} = 18.748$, $K_{12} = 7.548$, $\varphi = 16.71°$, $L_p = 0.071$ nH, and $C_p = 1.601$ pF. A comparison of their responses (simulated using AWR Design Environment) and the
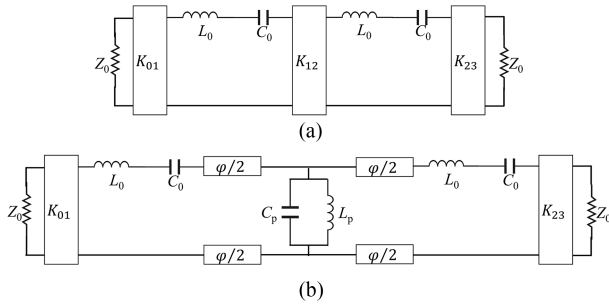
This article has been accepted for inclusion in a future issue of this journal. Content is final as presented, with the exception of pagination.

QIAN ET AL.: COMPACT MONOLITHIC 3D-PRINTED WIDEBAND FILTERS USING POLE-GENERATING RESONANT IRISES

FIGURE 4. Equivalent circuit model for the two-pole Chebyshev filter, based on (a) the ideal K-inverter and (b) the resonant Iris.
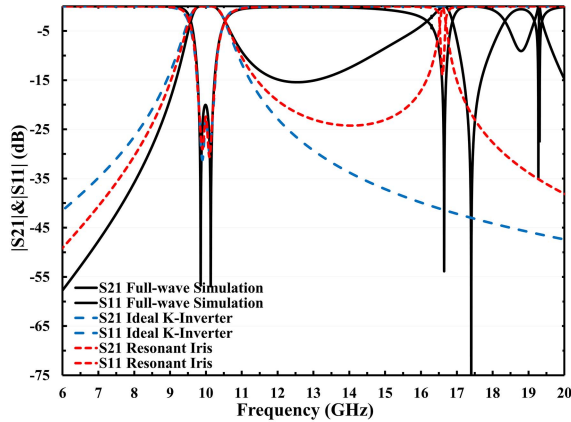

FIGURE 5. Comparison of filter performance of full-wave EM simulation, circuit simulation based on ideal K-inverter and resonant Iris.

FIGURE 6. Comparison of simulated third-order resonant Iris filter responses between filters with and without extra coupling Iris.

FIGURE 7. Coupling topology of the filter in Fig. 6 and the equivalent circuit of the singlet. X_{eq} and f_z are the equivalent slope parameter and the resonating frequency, respectively, of the series resonators determining the transmission zero; X_{nrn} is frequency-invariant reactance; and all $\Delta\varphi$ are the parameters of ideal phase shifters.

full-wave EM model response (from CST Microwave Studio) is shown in Fig. 5. It is apparent that the equivalent circuit with the resonant iris better represents the full-wave EM model in terms of the in-band response as well as the position of the transmission pole at 16.6 GHz.

2) CASE II: $(\omega_P = \omega_0)$

In this case, the resonant iris can be regarded as a singlet which produce a pole-zero pair in the frequency response. As demonstrated in [33], when the L-shaped resonant iris is sandwiched between two waveguide TE_{101} resonators, the TP generated by the resonance iris can be moved into the passband, as shown in Fig. 6 (the black solid curves) from a three-pole filter with one resonant iris. The transmission zero appears at 15 GHz. If an extra coupling aperture (See the inset of Fig. 6) is added next to the L-shaped iris, the TZ can be further controlled as shown in Fig. 6(the red dash curves). Three TPs are generated within the passband, while the TZ can be manipulated using the extra coupling iris. Therefore, the equivalent circuit in Fig. 3 is no longer applicable for the filter in this case. Considering its coupling topology (see Fig. 7), we can find the resonant iris not only provides the additional resonance node, but also allows the cross coupling k_{13}. The core pole-zero block (marked out by the red circle) is equivalent to a singlet. From the circuit perspective, the
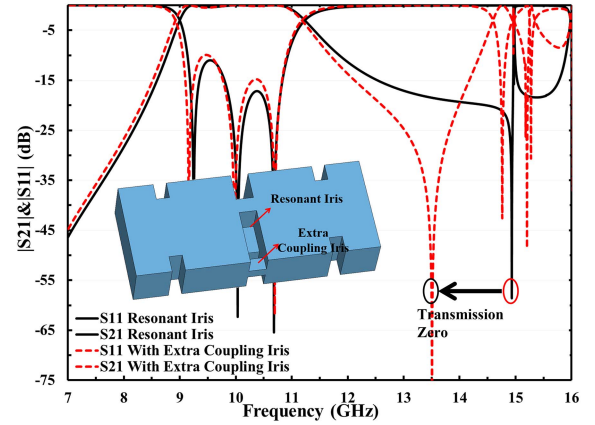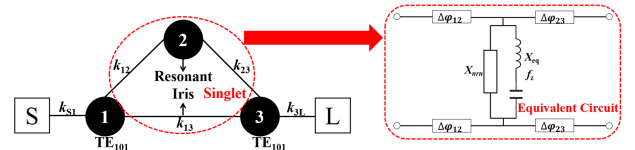
singlet can be more explicitly represented by the alternative equivalent circuit, as illustrated in Fig. 7 [38]. The shunt branch (series LC circuit) is added to account for the extra transmission zero. The synthesis-based approach to design filters with cascaded singlets has been well established [38], [39]. However, most methods are developed for narrowband filter and rely on circuit extraction process for physical implementation. Herein, we focus on the pole-generating feature of the resonant iris and use it to enhance the wideband capability of waveguide iris filters. In addition, the extra coupling iris allows us to control the cross-coupling. Thus, a more intuitive design approach is used to link the coupling coefficient to the real geometric dimensions of the resonant iris. Fig. 8 shows the EM simulation model and the simulated S_{21} response used to extract the coupling coefficient. According to [40], the frequencies of two peaks of S_{21} (f_{p1} and f_{p2}) represent the magnetic and electric frequency f_m and f_e. The corresponding coupling coefficient k can be calculated by

$$k = \pm \frac{f_{p1}^2 - f_{P2}^2}{f_{p1}^2 + f_{P2}^2} \tag{7}$$

where the plus-minus sign represents the different nature of the coupling, whether magnetic or electric. This can be further determined from the phase information of S_{21}. In each iteration of the simulation, both resonances should be adjusted to keep the average of the two peaks $(f_{p1} + f_{p2})/2$ at the specified centre frequency. In the simulation model, two SMA connectors are inserted into the resonators to provide the weak
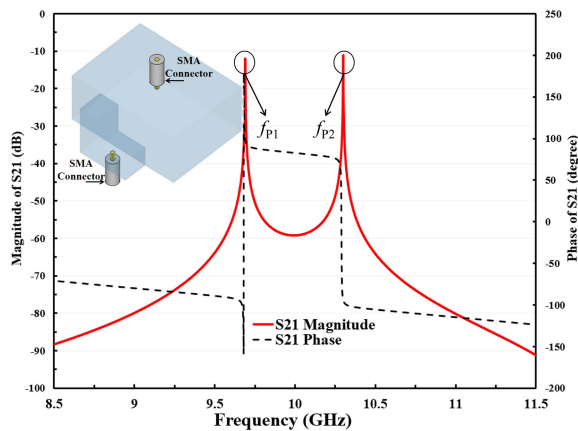
FIGURE 8. EM model used to extract coupling coefficient and the typical simulated transmission coefficient S21.
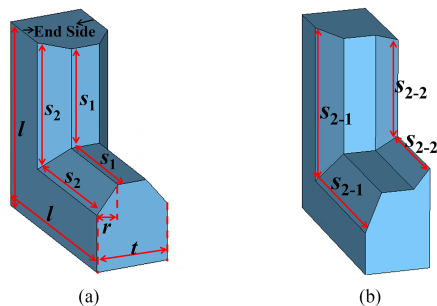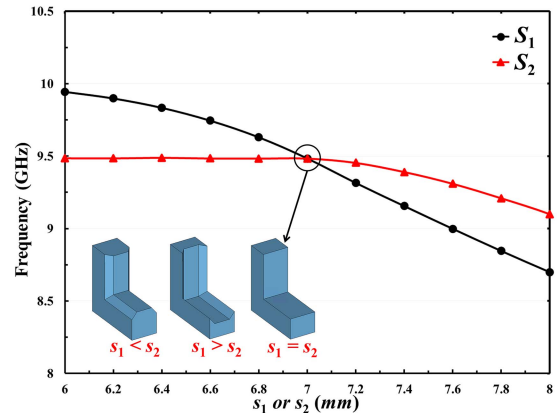

FIGURE 9. Modified resonant Iris structure and key dimension parameters. (a) Resonant Iris with symmetric couplings. (b) Resonant Iris with asymmetric couplings.

FIGURE 10. Parametric study of the resonant Iris. (a) Frequency variation versus s_1 or s_2, where one parameter is kept constant (7 mm) while the other is varied. (b) Frequency variation versus s_2 under different r/t.
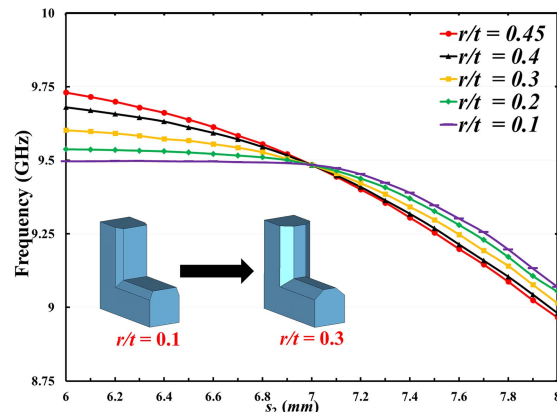
coupling. The open end of the resonant iris is approximated by a perfect magnetic wall to account for the loading effect from the adjacent resonator. It should be noted the model in Fig. 8 is simplified to illustrate the extraction process. More detail on the design of the resonant iris will be discussed in the next section.

C. OPTIMIZATION OF THE L-SHAPED RESONANT IRIS

It is often desired that the frequency and the coupling in a resonator can be adjusted seperately. However, for the primitive L-shpaed resonant iris (see Fig. 2(a)) proposed in [33], only two design parameters (t and s) can be used. The parameter l is largely fixed to fit the connected waveguide resonators. The degree of freedom in the design is very limited. New degree of freedom is needed for the resonant iris structure. Observing the simulated E-field distribution in Fig. 2, the E-field concentrates in the central area of the resonant structure and decays along to both sides. Therefore, the resonance frequency of the resonant iris is more sensitive to the dimensional changes of the structure in the central area. If we mitre the two end edges of the resonant iris, a taper transformation along the Z-axis can be formed, as shown in Fig. 9. As a result, an additional degree of freedom to control the frequency can be realized. This also facilitates the tuning of inter-resonator coupling with the adjacent resonators and the realization of asymmetric coupling.

Fig. 9(b) shows the tapered resonant iris with asymmetric coupling, where the two end sides have different cross-sections. It should be noted that such intricate structures would present significant difficulty with conventional machining. In contrast, they can be easily formed by 3-D printing.

Fig. 10 illustrates a few crucial dimensions of the modified resonant iris. The dimensions s_1 and s_2 are used to separately control the size of the middle and end cross-sections whereas the parameter r is used to control the angle of the mitred edges. It is important to note that the two mitered end sides can be different from each other to allow for asymmetric coupling. An example will be demonstrated later. Parametric studies were carried out to understand the behavior of the resonant iris. Both end sides are set as a perfect magnetic wall to imitate the loading effect, to some extent, from cascaded resonators. The parameter l is fixed to 10.16 mm to be compatible with the X-band waveguide. Fig. 10(a) shows the variation of the resonance frequency of the resonant iris versus s_1 or s_2, where the inset shows the air models of resonant iris at three representative cases. When s_1 equals to s_2, the modified resonant iris degenerates into the initial version. It is apparent that the resonance frequency is more sensitive to s_1, especially when
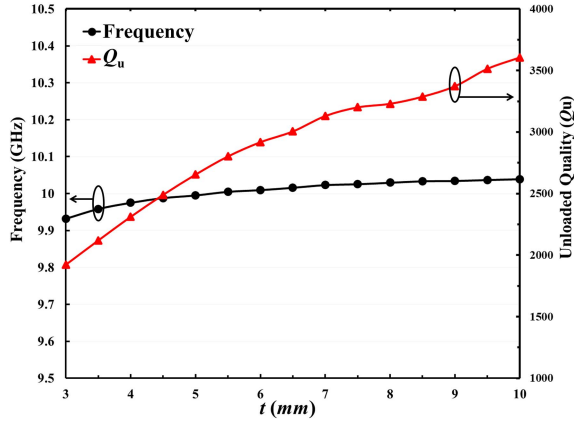
This article has been accepted for inclusion in a future issue of this journal. Content is final as presented, with the exception of pagination.

QIAN ET AL.: COMPACT MONOLITHIC 3D-PRINTED WIDEBAND FILTERS USING POLE-GENERATING RESONANT IRISES

FIGURE 11. Simulated resonance frequency and Q_u versus the thickness of the resonant Iris t.
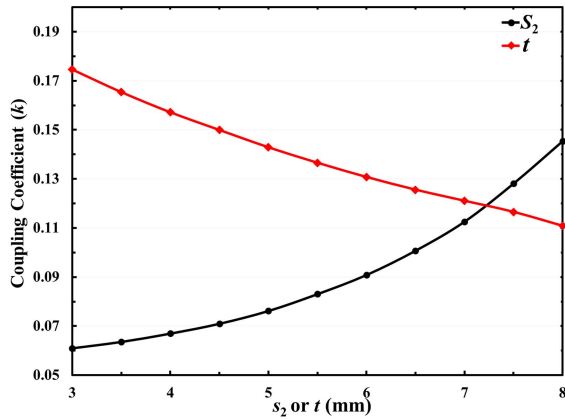

FIGURE 12. Simulated coupling coefficient versus the parameters s_2 and t.

s_2 is smaller than s_1. Further control can be applied by changing the parameter r. Shown in Fig. 10(b) is the variation of the resonance frequency versus s_2 under different ratio of r/t. As the ratio decreases, the frequency curve exhibits less variation, which means the ratio of r/t can mitigate the influence of s_2 on the resonance frequency. In addition, Fig. 11 shows the simulated resonance frequency and the unloaded quality factor Q_u versus the thickness of the resonant iris t. As can be observed, while the frequency change is almost negligible, the Q_u can be considerably improved with the increased thickness t. Still the Q_u of the resonant iris is smaller than the standard X-band rectangular waveguide resonator at 10 GHz (usually on the order of 8000) due to the condensed E-field. The electrical conductivity of silver (6.3×10^7 S/m) was assumed for the extraction of the Q_u.

Next, we consider the control of the coupling associated with the resonant iris, using the parameters s_2 and t. Fig. 12 shows the coupling coefficient curves, extracted using the method shown in Fig. 8. The coupling increases with the rising s_2 and decreases with t, while both parameters have comparable effect on the coupling strength. Therefore, the effective control of the coupling can be achieved by adjusting
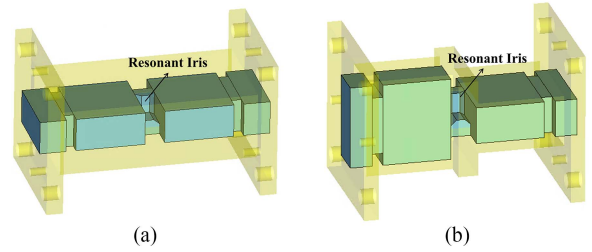

FIGURE 13. Internal structures of the third-order waveguide filters based on the pole-generating resonant Iris. (a) In-line configuration. (b) In-line configuration with polarization rotation.

the two parameters. Estimated from the achievable coupling strength, if we consider a common 4th-order Chebyshev filter, the achievable fractional bandwidth can readily reach at least 20%. Moreover, because of the field distribution of the L-shaped folded TE$_{101}$ mode is rotationally symmetric (see Fig. 2(a)), an additional polarization rotation feature can be realized. A filter with the rotation feature will be demonstrated later. It is worth noting that the resonant iris concept could work with other waveguide resonators than the rectangular cavity resonators used here.

Now that both the resonance frequency and coupling associated with the resonant iris are shown to be adjustable, the design procedure of the filter using resonant irises can be summarized as follows: 1) change the parameter s_1 to obtain the specified resonant frequency. In this step, s_2 equals to s_1; 2) adjust parameters s_2 and t to obtain the required coupling while fine-tuning s_1 and r to modify the resonance frequency; 3) construct the initial filter using the obtained dimensional parameters and then perform full-wave optimization.

III. DESIGN EXAMPLES
In this section, three filter prototypes are designed as demonstrators.

A. TWO THIRD-ORDER CHEBYSHEV FILTERS
Fig. 13 illustrates two third-order waveguide filters based on the pole-generating resonant iris, where an L-shaped resonant iris is sandwiched between two conventional TE$_{101}$ resonators. To aid visualization, the metallic wall of the filters is rendered with translucent yellow color. The first filter in Fig. 13(a) is with a traditional in-line configuration, whereas the filter in Fig. 13(b) is similar but with a polarization rotation feature where only the first resonator is rotated by 90°. All other dimensions are kept the same.

The first filter is specified with a centre frequency of 9 GHz, a fractional bandwidth of 9.5% and in-band return loss of 20 dB. The detailed discussion about this filter has been reported in [33]. Compared to the common rectangular waveguide filters, this filter has a footprint reduction of 20% while showing an improvement on the out-of-band rejection. The second example in Fig. 13(b) is to demonstrate the polarization rotation feature of the resonant iris. The same design specification as the first example is adopted. Fig. 14 compares the response
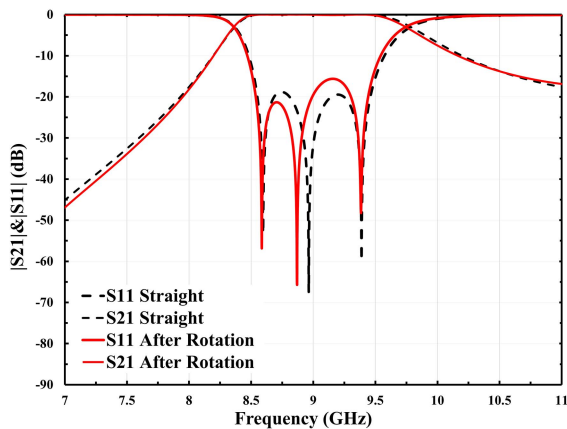
This article has been accepted for inclusion in a future issue of this journal. Content is final as presented, with the exception of pagination.

IEEE Journal of Microwaves

FIGURE 14. Simulation response of the third-order resonant iris filter with and without polarization rotation.

before and after polarization rotation. Little effect on the performance is shown, due to the rotation symmetry of the resonant iris.

B. A FIFTH-ORDER CHEBYSHEV FILTER

The third example is to demonstrate the wideband capability and the implementation of asymmetric coupling using the resonant iris. It is designed to operate at 10 GHz with the equal-ripple passband fractional bandwidth of 20% and a return loss of 20 dB. The design parameters can be calculated to be $k_{S1} = k_{5L} = 1.01$, $k_{12} = k_{45} = 0.86$, and $k_{23} = k_{34} = 0.63$. Fig. 15(a) shows the filter structure, where a tapered resonant iris was used to realize the asymmetric coupling on either side of the iris (i.e., $k_{12} \neq k_{23}$). Note that the mitred angle of the resonant iris in this example has been adjusted to provide a smoother transition between the two end faces. A comparison between the simulated and the ideal response calculated from coupling matrix is presented in Fig. 15(b). The response of the initial design from physical dimensioning (or coupling extraction) provided a reasonably good starting point for the following full-wave optimization. The filter response after optimization agrees well with the ideal response.

Fig. 16 compares the simulated wideband responses between the resonant iris filter and the conventional fifth-order waveguide iris filter, with the inset showing the their internal structure and the enlarged view of the in-band S_{21} responses. The 28% reduction in the overall length of the filter has been achieved. From Fig. 20(a), we can observe that the attenuation floor of the lower stopband is slightly worse than the rectangular waveguide filter. However, the upper stopband rejection is improved considerably over the waveguide iris filters as the spurious resonance mode is moved into the passband. The simulated insertion loss is 0.06 dB for the traditional and 0.15 dB for the resonant iris filter. The slightly higher loss is a result of the lower Q_u of the resonant iris. Another common concern about the low-Q resonant structure is the passband distortion, such as degraded passband flatness or rounded passband shoulder. To recover the sharp passband
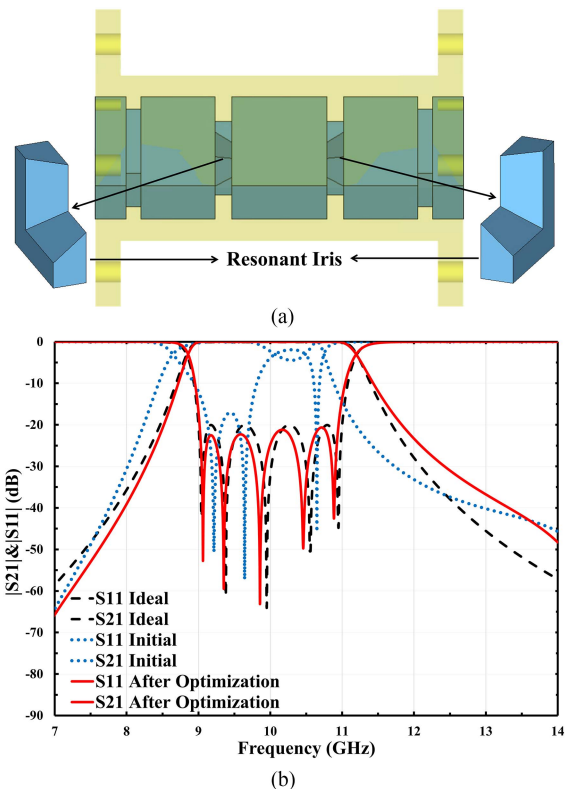

(a)

(b)

FIGURE 15. (a) Internal structure of a fifth-order waveguide filter based on the pole-generating resonant iris. (b) Comparison of filter responses: From extracted initial dimensions, after optimization, and from the ideal response determined by the coupling matrix.

selectivity, common methods include predistortion [41] and the use of nonuniform Q-values [42]. Connecting the external ports with a high-Q resonator is also an effective approach [43] in the practical application. For the proposed resonant iris filters, the low-Q resonant irises are sandwiched between two higher-Q rectangular waveguide resonators. There is some intrinsic balancing effect. From the expand view of the in-band S_{21} response (see Fig. 20(b)), we can see the variation in insertion loss are similar, around 0.2 dB, for the resonant iris filter and the conventional one. Therefore, it is reasonable to believe the resonant iris structure has a small impact on the in-band transmission response, especially for the wideband applications.

IV. MANUFACTURE AND MEASUREMENT
A. MANUFACTURING PROCESS

The resonant iris structure increases the manufacture complexity for traditional milling techniques, and even makes it impractical as far as the tapered resonant iris is concerned (Fig. 15). With this in mind, AM technique is chosen to manufacture the intricate tapered iris structure because of its unique capability of allowing monolithic fabrication of complex microwave components. More specifically, the selective laser melting (SLM) technique was employed on the twin-laser SLM500HL system. All three prototype designs were printed
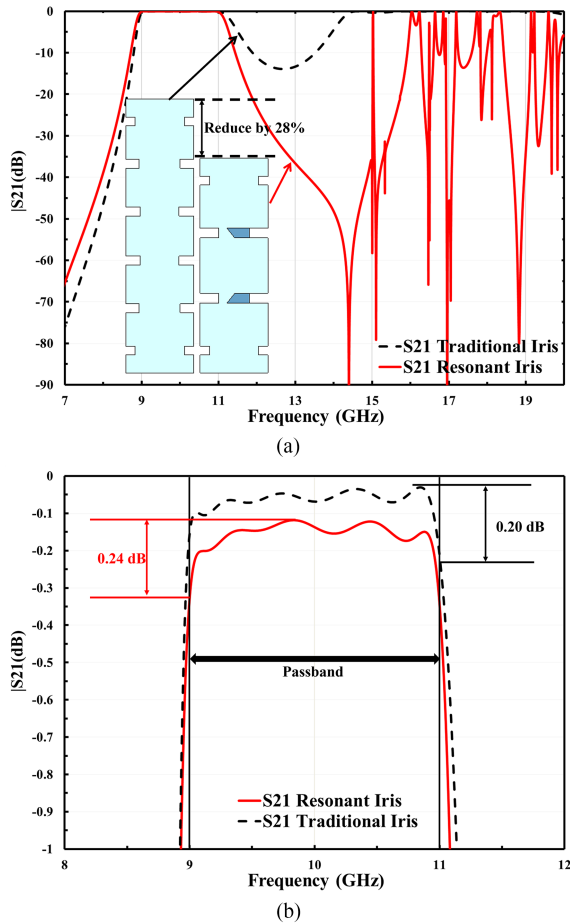
This article has been accepted for inclusion in a future issue of this journal. Content is final as presented, with the exception of pagination.

QIAN ET AL.: COMPACT MONOLITHIC 3D-PRINTED WIDEBAND FILTERS USING POLE-GENERATING RESONANT IRISES

(a)

(b)

FIGURE 16. Comparison of filter response between the traditional fifth-order waveguide filter and the filter based on pole-generating resonant iris. (a) Wideband response. (b) Enlarged view of the in-band response.
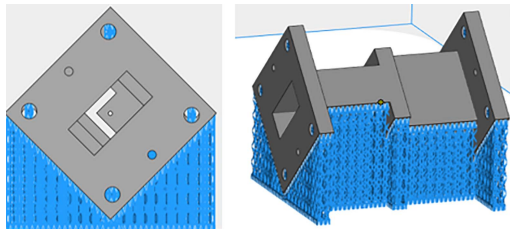

FIGURE 17. CAD model and external supporting structure (indicated in blue) used in the 3-D printing process.

monolithically using A20X. It is an aluminium-copper-based alloy powder, containing 92% aluminium, 5% copper, and 3% other materials. To examine the reproducibility of the manufacturing process, the 2nd and the 3rd design were printed twice. It should be noted they were printed in different batches to test the practical repeatability.

Fig. 17 illustrates the printing direction where the blue-coloured material represents the scaffold supporting structure. In printing, all the filters are tilted 45° to avoid any overhang structures inside the filter, while the downskin surface with the worst surface finish can be moved away from the electrical

TABLE 1. Processing Parameters of All Filters

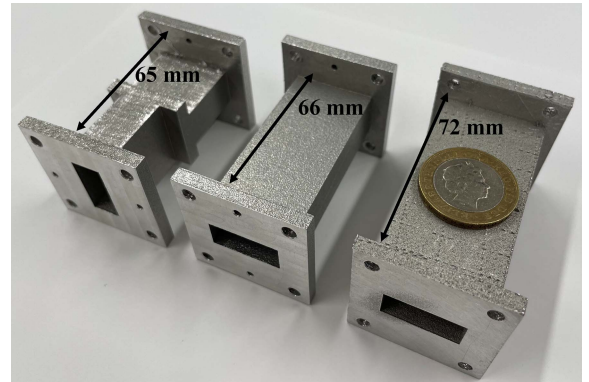| Powder Size (μm)	Layer Thickness (μm)	Laser power/P (W)	Scan speed/V (mm/s)	Spot size/h (μm)	Energy density/E (J/mm²)
15-53	30	360	1500	70-80	1.6

FIGURE 18. Photographs of three monolithically printed filters. From left to right, they are the third-order filter with polarization rotation, the third-order filter, and the fifth-order filter.

current concentrating area (top surface of rectangular waveguide). Table 1 summarizes the laser processing parameters and layer thickness. No surface treatment was applied on these samples except for the flange interfaces. Fig. 18 shows the photograph of the three monolithically printed filters. The small difference between the two third-order filters is caused by the length of feeding waveguide and wall thickness.

B. MEASUREMENT RESULTS

S-parameter measurements of all filters were performed on Agilent E8361C PNA network analyser. The analyser was calibrated using TRL (Thru, Reflect, Line) method prior to the measurements.

For 3-D printed devices, the effective electrical conductivity is significantly affected by the surface roughness. The first third-order filter was used to evaluate the effective conductivity of A20X alloy used in 3-D printing. Its nominal electrical conductivity has been reported to be 1.9×10^7 S/m [44]. Herein, the Hammerstad-Bekkadal (HB) method [45] is used to calculate the effective conductivity:

$$\sigma_e = \sigma_0 \times (K_{SR})^{-2} \tag{8}$$

where σ_0 is the electrical conductivity of the conductor with a smooth surface and K_{SR} is the Hammerstad correction factor, given by

$$K_{SR} = 1 + \frac{2}{\pi} \times \tan^{-1}\left(1.4 \times \left(\frac{\Delta}{\delta}\right)^2\right) \tag{9}$$

Here, δ is the skin depth of the conductor and Δ is the root mean square surface roughness. Δ of the printed filter in this
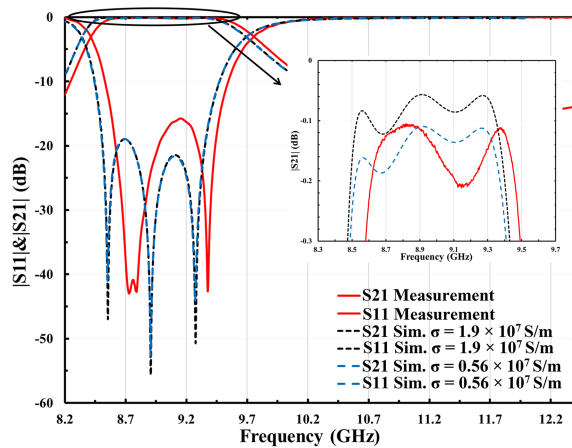
FIGURE 19. Comparison of the third-order resonant Iris filter between the measured result and simulation response with different electrical conductivities.

(a)

(b)

FIGURE 20. Measured and simulated results of all three examples. (a) Third-order filter with polarization rotation. (b) Fifth-order filter.

work was measured to be 3.5 μm using Alicona InfiniteFocusSL microscope. It is larger than the skin depth (1.2 μm for the A20X alloy at 9 GHz). The effective conductivity can be calculated to be 0.56×10^7 S/m.

To verify the calculated effective conductivity, Fig. 19 shows a comparison between the simulated results and the measured filter response, where the inset is the expanded view of S_{21}. It can be observed the surface roughness introduces an additional insertion loss of 0.07 dB. The measured insertion loss agrees well with that predicted from the effective conductivity, so the conductivity of 0.56×10^7 S/m will be applied in the following simulations to account for the impact of the surface roughness.

Fig. 20 shows the measured and simulated results of other two designs. No tuning was applied. As can be observed, all the measured passbands agree with the simulated results very well. For the third-order filter with polarization rotation, two samples were printed and measured (see Fig. 20(a)). The measured centre frequency is 8.91 GHz (Sample 1), shifted down by 1.0% and 9.05 GHZ (Sample 2), shifted up by 0.6%. Within the passband, the measured minimum return losses are around 15 dB whereas the measured average insertion loss is around 0.17 dB. The simulated insertion loss is 0.16 dB. Fig. 20(b) illustrates the in-band and wideband performance of the fifth-order waveguide filter. An excellent agreement is achieved between the simulated and measured in-band response, especially for the second sample. The measured centre frequency is 10.05 GHz and 9.97 GHz, respectively. The average insertion loss is better than 0.18 dB for both samples, which is close to the simulated 0.15 dB. The wideband performance is also as expected, with the rejection of 20 dB up to 15.3 GHz. It should be noted that 'response calibration' is used for the wideband measurement, so the evident ripple can be observed in the transmission response. Overall, very good agreement between the theoretical and measured results have been demonstrated.
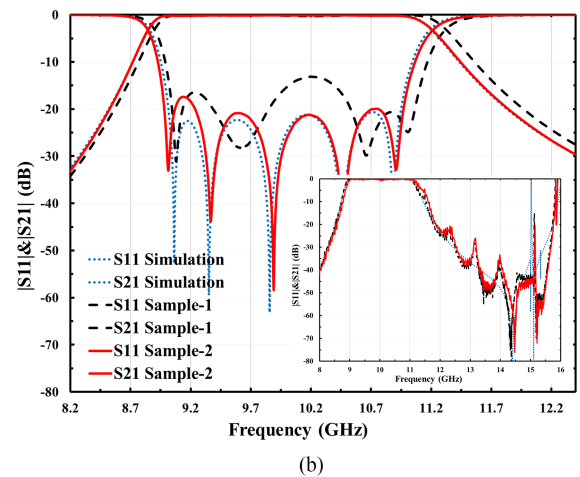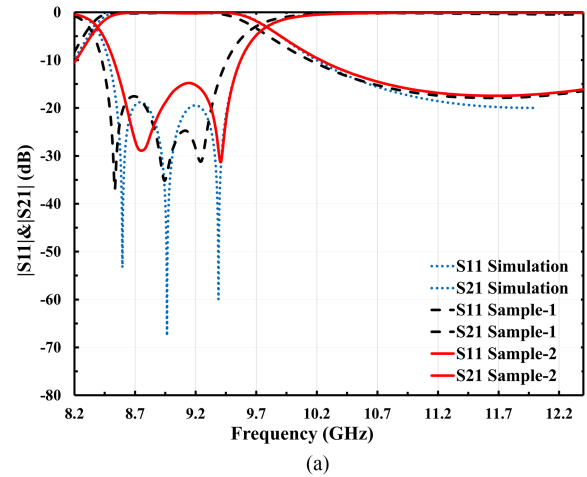
A reduced-Q resonant structure will set a lower bound on achievable minimum bandwidth. To evaluate this limit, we first extract the Q_u using coupling matrix method from the measurement responses of the two samples of the fifth-order filters. All resonators are assumed to be uniform for simplicity. The Q_u can be extracted to be 1700 (Sample 1) and 2100 (Sample 2). The average Q value of 1900 was then used to evaluate the insertion loss for filters with different bandwidths. If we consider the 1 dB threshold of insertion loss, the achievable bandwidth can be estimated to be 140 MHz. For typical filters in satellite payload around X-band, the resonant iris filters could be used for e wideband feeding filters (e.g., with a bandwidth of 250 or 500 MHz), but may not be suitable for the narrowband channel filters (e.g., with a bandwidth of 54 or 72 MHz).

To further investigate the reproducibility of the resonant iris structure using AM fabrication solution, a tolerance sensitivity analysis is carried out. Different from conventional CNC techniques where the tolerance is related to the practical milling process, the geometric error from 3-D printing is independent from the specific milling direction. Therefore, a tolerance

This article has been accepted for inclusion in a future issue of this journal. Content is final as presented, with the exception of pagination.

QIAN ET AL.: COMPACT MONOLITHIC 3D-PRINTED WIDEBAND FILTERS USING POLE-GENERATING RESONANT IRISES

TABLE 2. A Comparison With Some Wideband Filters

Ref.	Resonator Type	f_c (GHz)	FBW (%)	Average In-band Insertion loss (dB)	Spurious-free window (Rejection > 20dB)	Size (λ is the wavelength at the centre frequency f_c)	Number of Separate Blocks	Manufacture Technology
[1]	Multiple-mode cavity resonator	3.3	31	0.5	$1.5 \times f_c$	$(0.5 \times 0.5 \times 0.6)\lambda$	4	CNC
[2]	Single-mode dielectric resonator	3.9	13	0.14	$1.5 \times f_c$	$(0.4 \times 0.2 \times 0.2)\lambda$	9	CNC
[6]	Single-mode waveguide resonator	32.2	13.6	0.36	N/A	$(0.8 \times 0.4 \times 6.4)\lambda$	1	3-D Printing
[9]	Multiple-mode cavity resonator	25	20	0.67	$1.76 \times f_c$	$(1.8 \times 1.8 \times 1.3)\lambda$	2	3-D Printing
[18]	Single-mode resonant iris resonator	29.9	13	1	$1.4 \times f_c$	$(0.9 \times 0.4 \times 6.3)\lambda$	N/A	CNC
[19]	Single-mode resonant aperture resonator	7.6	19	0.19	$1.6 \times f_c$	$(0.6 \times 2.0 \times 5.2)\lambda$	2	CNC
[33]	Single-mode pole-generating iris resonator	9	10	0.15	$1.5 \times f_c$	$(0.7 \times 0.3 \times 1.8)\lambda$	1	3-D Printing
T.W.	Single-mode pole-generating iris resonator	10	20	0.17	$1.5 \times f_c$	$(0.8 \times 0.3 \times 2.4)\lambda$	1	3-D Printing

Ref: reference, f_c: central frequency, FBW: fractional bandwidth; CNC: computer numerical control; T. W.: this work.
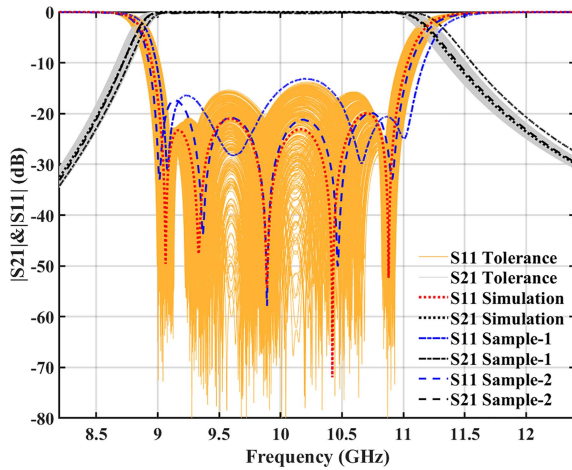
FIGURE 21. Sensitivity analysis of the fifth-order filter based on pole-generating resonant Iris.

sensitivity analysis based on Monte Carlo sampling method [46], [47] was performed on the fifth-order resonant iris filter. Six key dimensional parameters with $\pm 100~\mu$m (resolution of printing) tolerance were considered. 300 simulation samples with uniformly random distributed dimensions were taken. Fig. 21 shows the results of the sensitivity analysis, where the biggest frequency shift and worst return loss are 50 MHz and 15 dB, respectively. Both measurement results are within the envelope of the simulation samples. For the wideband application, we believe the 3-D printing technique is a reliable manufacture solution for the intricate pole-generating resonant iris structure.

Table 2 provides a comparison with published wideband filters. As can be observed, the resonant iris filter shows a wide bandwidth with competitive performance in insertion loss, out-of-band rejection, and miniaturization. The polarization rotation feature gives it more design flexibility.

V. CONCLUSION

In this paper, the design concept of a pole-generating resonant iris has been demonstrated using rectangular waveguide filters. By introducing the capacitive and inductive discontinuity simultaneously, a transmission pole can be generated by the L-shaped iris. A circuit analysis was performed to represent the operating mechanism. The prototype filters have demonstrated the capability of realizing a wider bandwidth of 20% while maintaining a compact footprint due to the miniature resonant iris. Improved out-of-band performance has also been shown. The polarization rotation feature has been shown in a 3rd-order filter. The major challenge associated with the resonant iris is its intricate structure and the almost inseparable feature from the cavity resonator, which makes it difficult to control the coupling. An approach to control and extract the coupling has been proposed. An intuitive design procedure was presented. The implementation of the filters is facilitated by 3-D printing technique. Very importantly, this allows the asymmetric coupling on either side of the resonant iris by using the tapered iris structure. The Q_u of the resonant iris is lower than traditional waveguide resonator, but in the wideband application this has limited impact on the insertion loss. All three filters were printed monolithically

This article has been accepted for inclusion in a future issue of this journal. Content is final as presented, with the exception of pagination.

IEEE Journal of
Microwaves

using SLM process. Excellent agreements between the simulated and measured results were achieved, which verifies the resonant iris concept, the design and manufacturing approach. The pole-generating resonant iris structure is not limited to rectangular waveguides and may be used for miniaturization or wideband applications. 3-D printing has proved to be a capable fabrication method for the resonant iris structures. Future work is expected on the design of more complex RF components, benefiting from the proposed resonant iris structure and the 3-D printing technique. The circuit synthesis method will be further developed.

ACKNOWLEDGMENT

REFERENCES

[1] S. W. Wong, S. F. Feng, L. Zhu, and Q.-X. Chu, "Triple- and quadruple-mode wideband bandpass filter using simple perturbation in single metal cavity," *IEEE Trans. Microw. Theory Techn.*, vol. 63, no. 10, pp. 3416–3424, Oct. 2015.

[2] J. Jiang and R. R. Mansour, "Wideband dielectric substrate-loaded cavity filter," *IEEE Trans. Microw. Theory Techn.*, vol. 68, no. 1, pp. 111–120, Jan. 2020.

[3] J.-C. Nanan, J.-W. Tao, H. Baudrand, B. Theron, and S. Vigneron, "A two-step synthesis of broadband ridged waveguide bandpass filters with improved performances," *IEEE Trans. Microw. Theory Techn.*, vol. 39, no. 12, pp. 2192–2197, Dec. 1991.

[4] Q. Zhang and Y. Lu, "Dimensional synthesis of symmetric wideband waveguide cross-coupled filters without global full-wave optimization," *IEEE Trans. Microw. Theory Techn.*, vol. 58, no. 12, pp. 3742–3748, Dec. 2010.

[5] Z. Li, P. Zhao, and K. L. Wu, "An I/O coupling multiplier circuit and its application to wideband filters and diplexers," *IEEE Trans. Compon., Packag. Manuf. Technol.*, vol. 8, no. 5, pp. 858–866, May 2018.

[6] J. Li, C. Guo, J. Xu, and L. Mao, "Lightweight low-cost Ka-band 3-D printed slotted rectangular waveguide bandpass filters," in *Proc. IEEE Antennas Propag. Soc. Int. Symp.*, 2017, pp. 2647–2648.

[7] C. Tomassoni, M. Dionigi, and R. Sorrentino, "Strategies for the improvement of the out of band behavior of TM dual-mode filters," in *Proc. IEEE 1st Int. Forum Res. Technol. Soc. Ind.*, 2015, pp. 90–93.

[8] S. F. Feng, S. W. Wong, L. Zhu, and Q. X. Chu, "A triple-mode wideband bandpass filter using single rectangular waveguide cavity," *IEEE Microw. Wireless Compon. Lett.*, vol. 27, no. 2, pp. 117–119, Feb. 2017.

[9] P. Vaitukaitis, K. Nai, J. Rao, M. S. Bakr, and J. Hong, "Technological investigation of metal 3D printed microwave cavity filters based on different topologies and materials," *IEEE Trans. Compon., Packag. Manuf. Technol.*, vol. 12, no. 12, pp. 2027–2037, Dec. 2022.

[10] I. C. Hunter, L. Billonet, B. Jarry, and P. Guillon, "Microwave filters–Applications and technology," *IEEE Trans. Microw. Theory Techn.*, vol. 50, no. 3, pp. 794–805, Mar. 2002.

[11] T. S. Chen, "Characteristics of waveguide resonant-Iris filters," *IEEE Trans. Microw. Theory Techn.*, vol. 15, no. 4, pp. 260–262, Apr. 1967.

[12] M. Piloni, R. Ravenelli, and M. Guglielmi, "Resonant aperture filters in rectangular waveguide," in *Proc. IEEE MTT-S Int. Microw. Symp.*, 1999, vol. 3, pp. 911–914.

[13] T. S. Chen, "Waveguide resonant-Iris filters with very wide passband and stopbands," *Int. J. Electron.*, vol. 21, no. 5, pp. 401–424, 1966.

[14] U. Rosenberg, S. Amari, and F. Seyfert, "Pseudo-elliptic direct-coupled resonator filters based on transmission-zero-generating irises," in *Proc. 40th Eur. Microw. Conf.*, 2010, pp. 962–965.

[15] M. Politi and A. Fossati, "Direct coupled waveguide filters with generalized Chebyshev response by resonating coupling structures," in *Proc. 40th Eur. Microw. Conf.*, 2010, pp. 966–969.

[16] U. Rosenberg and S. Amari, "A novel band-reject element for pseudoelliptic bandstop filters," *IEEE Trans. Microw. Theory Techn.*, vol. 55, no. 4, pp. 742–746, Apr. 2007.

[17] Y. Zhang, H. Meng, and K. L. Wu, "Direct synthesis and design of dispersive waveguide bandpass filters," *IEEE Trans. Microw. Theory Techn.*, vol. 68, no. 5, pp. 1678–1687, May 2020.

[18] R. M. Barrio-Garrido, S. Llorente-Romano, M. Salazar-Palma, A. Oñoro-Navarro, and I. Hidalgo-Carpintero, "Design, construction and experimental characterization of a broadband highly selective filter in waveguide technology in Ka-band," in *Proc. IEEE MTT-S Int. Microw. Symp.*, 2006, pp. 250–253.

[19] J. F. V. Sullca, S. Cogollos, V. E. Boria, and M. Guglielmi, "Compact dual-band and wideband filters with resonant apertures in rectangular waveguide," *IEEE Trans. Microw. Theory Techn.*, vol. 70, no. 6, pp. 3125–3140, Jun. 2022.

[20] R. Sorrentino and O. A. Peverini, "Additive manufacturing: A key enabling technology for next-generation microwave and millimeter-wave systems [point of view]," *Proc. IEEE*, vol. 104, no. 7, pp. 1362–1366, Jul. 2016.

[21] C. Tomassoni, O. A. Peverini, G. Venanzoni, G. Addamo, F. Paonessa, and G. Virone, "3D printing of microwave and millimeter-wave filters: Additive manufacturing technologies applied in the development of high-performance filters with novel topologies," *IEEE Microw. Mag.*, vol. 21, no. 6, pp. 24–45, Jun. 2020.

[22] P. Booth, J. Gilmore, E. V. Lluch, and M. Harvey, "Enhancements to satellite feed chain performance, testing and lead-times using additive manufacturing," in *Proc. 10th Eur. Conf. Antennas Propag.*, 2016, pp. 1–5.

[23] P. Martin-Iglesias, M. Van Der Vorst, J. Gumpinger, and T. Ghidini, "ESA's recent developments in the field of 3D-printed RF/microwave hardware," in *Proc. 11th Eur. Conf. Antennas Propag.*, 2017, pp. 553–557.

[24] C. Guo, J. Li, X. Shang, M. J. Lancaster, and J. Xu, "Progress on microwave devices fabricated using stereolithography 3-D printing technique," in *Proc. Int. Appl. Comput. Electromagn. Soc. Symp. China*, 2017, pp. 1–2.

[25] M. Salek, X. Shang, and M. J. Lancaster, "Compact S-band coaxial cavity resonator filter fabricated by 3-D printing," *IEEE Microw. Wireless Compon. Lett.*, vol. 29, no. 6, pp. 382–384, Jun. 2019.

[26] P. Vaitukaitis, K. Nai, J. Rao, and J. Hong, "On the development of metal 3D printed bandpass filter with wide stopband based on deformed elliptical cavity resonator with an additional plate," *IEEE Access*, vol. 10, pp. 15427–15435, 2022.

[27] P. Booth and E. V. Lluch, "Enhancing the performance of waveguide filters using additive manufacturing," *Proc. IEEE*, vol. 105, no. 4, pp. 613–619, Apr. 2017.

[28] O. A. Peverini et al., "Integration of an *H*–plane bend, a twist, and a filter in Ku/K-Band through additive manufacturing," *IEEE Trans. Microw. Theory Techn.*, vol. 66, no. 5, pp. 2210–2219, May 2018.

[29] P. Booth, R. Roberts, M. Szymkiewicz, and C. Hartwanger, "Using additive manufacturing for feed chain and other passive microwave components," in *Proc. 11th Eur. Conf. Antennas Propag.*, 2017, pp. 558–562.

[30] C. Guo et al., "A 3-D printed *E*–plane waveguide magic-T using air-filled coax-to-waveguide transitions," *IEEE Trans. Microw. Theory Techn.*, vol. 67, no. 12, pp. 4984–4994, Dec. 2019.

[31] L. Qian et al., "Thermal stability analysis of 3D printed resonators using novel materials," in *Proc. 51st Eur. Microw. Conf.*, 2022, pp. 334–337.

[32] X. Wen et al., "An invar alloy SLM printed diplexer with high thermal stability," *IEEE Trans. Circuits Syst. II, Exp. Briefs*, vol. 69, no. 3, pp. 1019–1023, Mar. 2022.

[33] L. Qian, R. Martinez, M. Salek, M. Attallah, Y. Wang, and M. J. Lancaster, "Compact monolithic SLM 3D-printed filters using pole-generating resonant Irises," in *Proc. 51st Eur. Microw. Conf.*, 2022, pp. 118–121.

[34] C. Lopez, V. Desmaris, D. Meledin, A. Pavolotsky, and V. Belitsky, "Design and implementation of a compact 90° waveguide twist with machining tolerant layout," *IEEE Microw. Wireless Compon. Lett.*, vol. 30, no. 8, pp. 741–744, Aug. 2020.

[35] L. Zeng, C. E. Tong, S. N. Paine, and P. K. Grimes, "A compact machinable 90° waveguide twist for broadband applications," *IEEE Trans. Microw. Theory Techn.*, vol. 68, no. 7, pp. 2515–2520, Jul. 2020.

[36] J. Q. Ding, Y. Zhao, and S. C. Shi, "A full WR-3 band and low-loss 90° waveguide twist based on CNC," *IEEE Trans. THz Sci. Technol.*, vol. 10, no. 1, pp. 93–96, Jan. 2020.

[37] G. Barué, *Microwave Engineering*. Hoboken, NJ, USA: Wiley, 2008.

[38] G. Macchiarella, G. G. Gentili, C. Tomassoni, S. Bastioli, and R. V. Snyder, "Design of waveguide filters with cascaded singlets through a synthesis-based approach," *IEEE Trans. Microw. Theory Tech.*, vol. 68, no. 6, pp. 2308–2319, Jun. 2020.

[39] G. Macchiarella et al., "Accurate modeling of stubs used as resonant coupling elements in SIW filters," *IEEE Microw. Wireless Compon. Lett.*, vol. 30, no. 12, pp. 1125–1128, Dec. 2020.

[40] J.-S. Hong and M. J. Lancaster, *Microstrip Filters for RF/Microwave Applications*. Hoboken, NJ, USA: Wiley, 2004.

[41] M. Dishal, "Design of dissipative band-pass filters producing desired exact amplitude-frequency characteristics," *Proc. Inst. Radio Engineers*, vol. 37, no. 9, pp. 1050–1069, Sep. 1949.

[42] A. C. Guyette, I. C. Hunter, and R. D. Pollard, "The design of microwave bandpass filters using resonators with nonuniform Q," *IEEE Trans. Microw. Theory Techn.*, vol. 54, no. 11, pp. 3914–3921, Nov. 2006.

[43] J. Hong, J. NI, and M.-I. Petronilo, "A radio frequency pass-band filter," Patent WO2020057722A1, Sep. 17, 2018.

[44] A. M. Howatson, P. G. Lund, and J. D. Todd, *Engineering Tables and Data*. Berlin, Germany: Springer, 2012.

[45] E. Hammerstad and O. Jensen, "Accurate models for microstrip computer-aided design," in *IEEE MTT-S Int. Microw. Symp. Dig.*, 1980, pp. 107–409.

[46] Z. Zhang, H. Chen, Y. Yu, F. Jiang, and Q. S. Cheng, "Yield-constrained optimization design using polynomial chaos for microwave filters," *IEEE Access*, vol. 9, pp. 22408–22416, 2021.

[47] X. Wen et al., "SLM printed waveguide dual-mode filters with reduced sensitivity to fabrication imperfections," *IEEE Microw. Wireless Compon. Lett.*, vol. 31, no. 11, pp. 1195–1198, Nov. 2021.

LU QIAN (Graduate Student Member, IEEE) was born in Hunan, China. He received the B.Eng. degree (Hons.) in information engineering and the M.S. degree in information and communication system from the South China University of Technology, Guangzhou, China, in 2016 and 2019, respectively. He is currently working toward the Ph.D. degree in electronic engineering with the University of Birmingham, Birmingham, U.K.

His research interests include microwave filters, multiport coupled-resonator network, and 3-D printed microwave devices.

RAFAEL MARTINEZ received the M.Sc. degree in advanced manufacturing technologies and the Ph.D. degree in mechanical engineering in additive manufacturing from the University of Sheffield, Sheffield, U.K., in 2013 and 2019, respectively.

He is currently additive manufacturing technology officer with the University of Birmingham, Birmingham, U.K.

MILAN SALEK received the B.Eng. degree in electrical and electronic engineering from Aston University, Birmingham, U.K., in 2016, and the Ph.D. degree in microwave engineering from the University of Birmingham, Birmingham, U.K., in 2019.

Following graduation, he continued to work as a Research Fellow with the Department of Electronic, Electrical and Systems Engineering, University of Birmingham. He is currently a RF Microwave Engineer with QinetiQ, Malvern, U.K. His research interests include passive and active microwave devices, bolometric and diode-based power sensors, reconfigurable antennas, and millimeterwave and terahertz circuits.

TALAL SKAIK received the M.Sc. degree in communications engineering and the Ph.D. degree in microwave engineering from the University of Birmingham, Birmingham, U.K., in 2007 and 2011, respectively.

After his Ph.D. degree, he was a lecturer of electrical engineering till 2019. He is currently a Research Fellow with the Department of Electronic, Electrical and Systems Engineering, the University of Birmingham. He has authored or coauthored m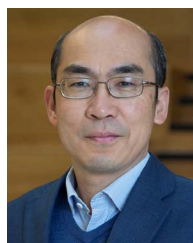ore than 30 refereed research papers. His research interests include millimeter-wave and terahertz filters and antennas, 3D-printed microwave devices, temperature compensated filters for satellite payloads, and multiport coupled resonator structures. He acts as a reviewer for various microwave journals and for the European Microwave Conference (EuMC).

MOATAZ ATTALLAH received the Ph.D. degree in metallurgy and materials science from the University of Birmingham, Birmingham, U.K., in 2007.

He is a Professor of advanced materials processing with the School of Metallurgy and Materials, University of Birmingham. He coauthored more than 200 journal and conference papers, three book chapters, and is a co-inventor on five patents. His research focuses on developing a metallurgical understanding of the material-process interaction in additive manufacturing of metallic materials focusing on the process impact on the microstructure and structural integrity development. His research is conducted through research partnerships with various companies in the aerospace, medical, space, and nuclear energy sectors.

YI WANG (Senior Member, IEEE) was born in Shandong, China. He received the B.Sc. degree in applied physics and the M.Sc. degree in condensed matter physics from the University of Science and Technology, Beijing, China, in 1998 and 2001, respectively, and the Ph.D. degree in electronic and electrical engineering from the University of Birmingham, Birmingham, U.K., in 2005.

From 2004 to 2011, he was a Research Fellow with the University of Birmingham. In 2011, he became a Senior Lecturer and then Reader with the University of Greenwich, U.K. He is currently an Associate Professor with the University of Birmingham. He leads the Emerging Device Technology (EDT) Research Lab, specializing in the application of new materials and advanced manufacturing techniques to high frequency devices. He is also the Academic Lead of the Engineering Cleanroom and the Terahertz Measurement Facility, Birmingham. He is the author of more than 210 research papers and has been an Associate Editor for IET MAP. He was the TPC Chair of 2021 European Microwave Conference. His research interests include 3D printed microwave and mm-wave devices, waveguide antenna technology, multiport filtering networks, filter-antenna integration, millimeter-wave and sub-terahertz antennas and devices for metrology, communication, and sensing. He is particularly interested in working with new materials and novel manufacturing techniques for RF/microwave applications.